JEE Journal of Ecological Engineering

Journal of Ecological Engineering, 2026, 27(7), 109–124
https://doi.org/10.12911/22998993/218292
ISSN 2299–8993, License CC-BY 4.0

Received: 2026.01.17
Accepted: 2026.05.20
Published: 2026.06.01

Innovative coconut frond-derived activated carbon for treating acid mine drainage

Esthi Kusdarini[1*], Skolastika Margareth Onofrisan[1], Yudho Dwi Galih Cahyono[1], Agus Budianto[2]

[1] Department of Mining Engineering, Faculty of Industrial Technology, Institut Teknologi Adhi Tama Surabaya, 60117, Indonesia
[2] Department of Chemical Engineering, Faculty of Industrial Technology, Institut Teknologi Adhi Tama Surabaya, 60117, Indonesia
* Corresponding author's e-mail: esti@itats.ac.id

ABSTRACT

This study investigated the synthesis and adsorption performance of activated carbon derived from coconut fronds for the removal of iron (Fe) and manganese (Mn) from acid mine drainage (AMD). The adsorbent was prepared by chemical activation with hydrochloric acid (HCl), followed by thermal activation at 923 K. Physicochemical characterization included proximate analysis, Brunauer–Emmett–Teller (BET) surface area, iodine value, pore structure analysis, and Fourier Transform Infrared (FTIR) spectroscopy. The activated carbon exhibited a high fixed carbon content (75.9%), a BET surface area of 394.78 $m^2 g^{-1}$, an average pore diameter of 6.91 nm, and an iodine value of 1130.26 mg g^{-1}, indicating a well-developed porous structure. FTIR analysis confirmed the presence of oxygen-containing functional groups, particularly C–O, which contribute to the adsorption of metal ions. The researcher experiments with batch adsorption using modified acid mine drainage with Fe and Mn concentrations of 300–600 mg L^{-1} and contact times of 10–80 min. The equilibrium data were better described by the Freundlich isotherm model, with R^2 values of 0.937 for Fe and 0.955 for Mn, indicating multilayer adsorption on heterogeneous surfaces. The maximum adsorption capacities were 95.85 mg g^{-1} for Fe and 9.31 mg g^{-1} for Mn. The kinetic analysis followed a pseudo-second-order model. The researcher achieved removal efficiencies of 83.33% for Fe and 66.88% for Mn, demonstrating the strong potential of coconut frond-based activated carbon as a low-cost adsorbent for AMD treatment.

Keywords: acid mine drainage, activated carbon, coconut fronds, iron, manganese.

INTRODUCTION

Access to clean water is a fundamental human right and an essential pillar for public health and sustainable development. These principles are recognized globally through the United Nations Sustainable Development Goals, particularly Goals 6 (clean water and sanitation) and 3 (good health and well-being). However, achieving these goals is hampered by various anthropogenic activities, including mining operations, which are significant contributors to water pollution. Communities living around mining areas often face severe consequences from acid mine drainage, a persistent environmental problem, and the degradation of freshwater resources. Previous research has shown that acid mine drainage has contaminated karst rivers in Southwest China, causing river water containing Fe, Mn, Ni, and AS to exceed WHO quality standards, thereby increasing health risks for children. Several methods have been developed to prevent acid mine drainage, including capillary barriers (Fanani et al., 2025; Hao et al., 2026; Meng et al., 2025). However, if acid mine drainage persists, treatment must be carried out.

Acid mine drainage is produced when sulphide-containing minerals, exposed to air and water during mining activities, undergo oxidation, forming sulfuric acid. These acidic wastes

dissolve heavy metals and other elements from surrounding rocks, yielding solutions with low pH and high concentrations of toxic metals. The metal content and pH of acid mine drainage vary with the seasons and with hydrogeochemical conditions and metal fluxes. Among these metal contaminants, iron (Fe) and manganese (Mn) are usually the most common and problematic in acid mine drainage (Camargo et al., 2026; Singer et al., 2026; Kusdarini et al., 2023, 2024).

The prevalence of Fe and Mn in acid mine drainage is directly related to the mineralogy of the mining area. Highlighting the acidification process, mineralogy evidence of acid mine drainage in coal mine waste heaps in the Nord Pas-de-Calais coal mining basin (Northern France), the formation of secondary minerals typical of AMD (Acid Mine Drainage), and the release of elements from rock fragments explain their potential to form acid mine drainage Iron is commonly found in minerals such as pyrite (FeS_2), siderite ($FeCO_3$), hematite (Fe_2O_3), and goethite (FeOOH). In contrast, manganese is often found in pyrolusite (MnO_2), psilomelana [$(Ba, H_2O)_2Mn_5O_{10}$], and rhodochrosite ($MnCO_3$). In acidic conditions, these metals dissolve, thereby mobilizing them into water bodies. The presence of high levels of Fe and Mn in water causes various adverse effects. This condition leads to aesthetic issues, including water discolouration, a metallic taste, and turbidity. From an ecological and health perspective, these metals are alarming. Manganese is a neurotoxin, and chronic exposure is associated with neurological disorders. Although essential in small amounts, excessive Fe can damage aquatic ecosystems and infrastructure through precipitation, lowering oxygen levels, and clogging waterways. Therefore, effective removal of Fe and Mn from acid mine drainage is essential to protect environmental and human health (Chen et al., 2026; Sales et al., 2025).

The removal of Fe and Mn from acid mine drainage can be achieved using several methods, including physical, chemical, and biological. Fe removal using biological processes, namely Chlorella vulgaris microalgae. However, this method for extreme conditions requires a relatively long time, and is dependent on light and nutrients. Treatment of acid mine drainage using other biological methods involves using iron-oxidizing bacteria (*Acidithiobacillus* and *Acidiphilium*) and manganese-oxidizing bacteria (*Azospirillum* and *Acinetobacter*). This Method can remove Fe(II), Mn(II), and Cu(II) up to 90% (Mao et al., 2026). The use of Firmicutes and Actinobacteria has also been shown to reduce sulphates in acid mine drainage by up to 70%. The use of an extreme acidophilic bacterium, *Virgibacillus pantothenticus* WL, isolated directly from AMD, demonstrated remarkable innate tolerance, growing at pH 3.0 and Cu(II) concentrations up to 200 mg L^{-1}. *V. pantothenticus* WL achieved high Cu(II) removal efficiencies of 85% and 80% of Cu(II) solutions of 100 mg L^{-1} and 200 mg L^{-1} through a continuous process. Such removal is mediated by a synergistic mechanism in which bacterial sulphate reduction precipitates Cu(II) as a stable sulphide mineral (chalcopyrite and covelite). At the same time, simultaneous metabolic activity increases the system pH, thereby activating the metal-binding capacity of extracellular polymeric substances for improved biosorption (Lin et al., 2025; Han et al., 2026).

Other findings suggest that AMD's fuel cell system (AMD-FC) was developed based on the principle of electrochemical oxidation, achieving the dual goals of Fe^{2+} removal and energy recovery while enabling the recovery of anodic deposits as a valuable resource. The results showed that under optimal conditions, the batch mode achieved a power density of 83.66 mW m^{-2} and an Fe removal rate of 84.6%. The recirculation mode maintains power generation for 15 hours, with Fe removal exceeding 80%. The electrochemical oxidation method is quite effective, providing two benefits: generating electrical energy and removing Fe from acid mine drainage. However, this method has relatively high investment costs, complex operations and maintenance, and is challenging to implement on an industrial scale (Ren et al., 2025). In addition to biological and electrochemical oxidation methods, several conventional methods for removing Fe and Mn from water include filtration, ion exchange, coagulation-flocculation, and chemical precipitation. However, these techniques often have limitations, including high operational costs, significant chemical sludge formation, and inefficiencies at low metal concentrations. Instead, adsorption techniques have become a practical, efficient, and potentially economical option. The effectiveness of adsorption depends on the development of high-performance adsorbents (Khumalo et al., 2025; Kusdarini et al., 2020, 2021; Kusdarini et al., 2021; Kusdarini et al., 2023; Tao et al., 2026; Kusdarini, et al., 2025; Kusdarini et al., 2025; Kusdarini and Budianto, 2022; Moyo et al., 2025; Wibowo et al., 2024).

In recent years, research has shifted toward using low-cost, renewable materials, especially agricultural waste, to produce biochar. This approach addresses waste management issues while creating value-added products for environmental remediation. Various agrarian waste products, such as rice husks, coconut shells, palm shells, and lemongrass, have been successfully converted into effective adsorbents for heavy metals. The use of manganese and quinizarin impregnated BiochaBiochartificial wetlands can efficiently reduce the content of Al, Fe, Cu, Zn, and As (Budianto et al., 2021; Budianto et al., 2023; Budianto et al., 2021; Budianto et al., 2021; Kusdarini et al., 2025; Kusdarini et al., 2025; Atilano-Camino et al., 2026).

Despite progress in bio-adsorbent development, the increasing demand for effective, affordable materials necessitates the exploration of new, abundant, and underutilized lignocellulose precursors. One of these promising materials is coconut fronds. Indonesia is one of the largest coconut-producing countries in the world, with coconut plantation areas spread widely in coastal and rural areas. Although previous research has explored a variety of agricultural wastes, the specific development of activated carbon from coconut fronds for simultaneously removing Fe and Mn from acid mine drainage remains underexplored (Younis Al-Ani et al., 2026).

This research aims to bridge this gap by comprehensively developing and evaluating new adsorbents derived from coconut fronds (ACCF) for the treatment of acid mine drainage. The novelty of this research lies in the optimization of ACCF synthesis through chemical activation (using HCl), followed by thermal activation at 923 K, and its subsequent application for the removal of Fe and Mn in AMD. Its performance was evaluated through batch adsorption studies, with kinetic and isothermal analyses providing insight into the underlying mechanisms. This research not only offers a sustainable solution for AMD remediation but also contributes to increasing the value of agricultural waste, in line with circular economy principles.

Table 1. Parameters of acid mine drainage

No	Parameter	Acid mine drainage	Unit
1	pH	5.6	-
2	Total suspended solid	24.7	mg L^{-1}
3	Fe	4.24	mg L^{-1}
4	Fixed carbon (%)	2.08	mg L^{-1}

MATERIALS AND METHODS

Materials and tools

The materials used in this study were samples of acid mine drainage from mining areas in South Sumatra, coconut fronds (Cocos nucifera L. var. typica), HCl, NaOH, $FeCl_2$, $MnSO_4$, amylum, iodine, Na_2SO_3, and distilled water. Coconut fronds were selected as raw materials due to their local availability and high lignocellulosic content. Meanwhile, the tools used include saws, mixers, sieves, analytical balances, drip pipettes, measuring flasks, clamps, filter paper, burettes, furnaces, beaker glass, aluminum foil, funnels, measuring cups, and Erlenmeyer flasks. The characteristics of the acid mine drainage are presented in Table 1.

Research procedure

Methodological sequence research starting from (i) raw material preparation, (ii) chemical activation using HCl, (iii) thermal activation at 923 K, (iv) physicochemical characterization (proximate analysis, BET surface area, iodine value, pore structure, and FTIR), followed by (v) batch adsorption experiments, and (vi) data analysis using isotherm and kinetic models.

Making activated carbon from coconut fronds (ACCF)

The making of ACCF includes several steps: 1) drying the coconut fronds dry, then cutting them into pieces with a size of 3–4 cm, 2) carbonization, heating the coconut fronds in a furnace at a temperature of 573 K for 3 hours, 3) smoothing, smoothing the coconut fronds that have been carbonized using a mixer, then sifting with a 60 mesh sieve, 4) chemical activation, soaking the charcoal in a 1 M HCl solution for 7 hours, washing with NaOH 0.1 M and distilled water to neutral pH, separating the charcoal from the solution with filter paper, 5) physical activation, heating the charcoal in the furnace at a temperature of 923 K for 15 minutes (Figure 1).

Activated carbon characteristic test

Testing of activated carbon parameters after chemical activation and after chemical-physical activation includes: 1) water content testing (ASTM D-3173-92), 2) volatile matter content

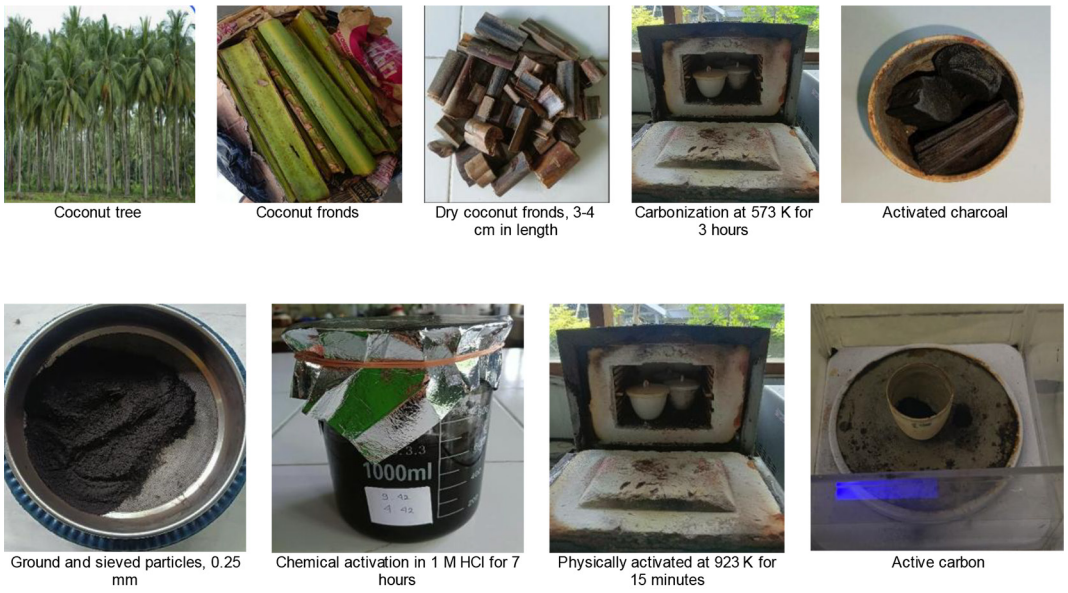

Figure 1. Preparation of activated carbon from coconut fronds

(BS-1016), 3) ash content (ASTM D-3174-98), 4) iodine number (ASTM D-4607-94), 5) BET (Anton Paar Kaomi for Nova), 6) SEM EDS, 7) FTIR. Furthermore, fixed carbon is calculated using Equation 1.

$$\textit{Water content} + \textit{volatile matter} + \textit{ash content} + \\ + \textit{fixed carbon} = 100\% \quad (1)$$

Testing of ACCF's adsorption power against Fe and Mn

The ability of ACCF to adsorb Fe(II) and Mn(II) ions in modified acid mine drainage was tested using Fe(II) and Mn(II) ion concentration variables. In contrast, contact time variables were utilized for Mn(II) ions.

Fe concentration variables

A test with a concentration variable was carried out by adding 2.4 g of ACCF to 1 L of Fe concentration modified acid mine drainage of 600 mg L^{-1} (FeI_1 sample), 525 mg L^{-1} (FeI_2 sample), 450 mg L^{-1} (FeI_3 sample), 375 mg L^{-1} (FeI_4 sample), and 300 mg L^{-1} (sample FeI_5), stirred at 120 rpm for 40 minutes, then the acid mine drainage sample was separated from the ACCF and the Fe content was analyzed using the AAS method.

Mn concentration variables

Testing with variable concentrations was carried out by adding ACCF as much as 2.4 g to 1 L of Min-based amino acid water with a concentration of 600 mg L^{-1} (MnI_1 sample), 525 mg L^{-1} (MnI_2 sample), 450 mg L^{-1} (MnI_3 sample), 375 mg L^{-1} (MnI_4 sample), and 300 mg L^{-1} (sample MnI_5), stirred at 120 rpm for 40 minutes, then the sample was separated from ACCF and analyzed for Mn content using the AAS method.

Contact time variables

Variable contact time testing was carried out by inserting 2.4 g of ACCF into 1 L of Mn solution with a concentration of 600 mg L^{-1}, stirred at 120 rpm for 10 minutes (sample Mnk_1), 20 minutes (sample Mnk_2), 40 minutes (sample Mnk_3), 60 minutes (sample Mnk_4), 80 minutes (sample Mnk_5). The samples were separated from ACCF, and AAS analyzed the Mn content.

The ability of ACCF to remove metals is expressed in the % removal presented in Equation 2.

$$\%\ removal = \frac{C_t - C_0}{C_0} \cdot 100\% \quad (2)$$

where: *Co* is the concentration of Mn in modified aminic acid water before contact with ACCF (mg L^{-1}), and *Ct* is the concentration of Mn in modified aminic acid water after contact with ACCF (mg L^{-1}).

The Freundlich equation

The Freundlich isothermal adsorption equation is presented in Equation 3.

$$\log q_e = \log k_f + \frac{1}{n} \log c_e \quad (3)$$

where: *qe* is the mass of adsorbed metal ions per unit mass of ACCF (mg g^{-1}), k_f is the Freundlich constant ((mg g^{-1})(L mg^{-1})^(n^{-1})), *n* is the empirical parameter, and c_e is the concentration of dissolved metal ions under equilibrium conditions (mg L^{-1}).

From Equation 1 and the results of the AAS test, the constants k_f and n will be obtained.

The Langmuir equation

The Langmuir isothermal adsorption equation is presented in Equation 4.

$$q_e = \frac{q_{max} K_L C_e}{1 + K_L C_e} \quad (4)$$

where: q_e – amount of adsorbed adsorbate at a balanced state (mg g^{-1}); c_e – concentration of adsorbate in solution at equilibrium (mg L^{-1}); q_{max} – maximum capacity of monolayer adsorption (mg g^{-1}), and K_L – Langmuir constant (L mg^{-1}), indicating surface affinity to adsorbate.

To determine the value, the Langmuir equation is often written experimentally as:

$$\frac{C_e}{q_e} = \frac{1}{K_L q_{max}} + \frac{C_e}{q_{max}} \quad (5)$$

The result of the linear regression of the graph $\frac{C_e}{q_e}$ against C_e will be obtained Slope = $\frac{1}{q_{max}}$ and Intercept (y-axis cut-off point) = $\frac{1}{K_L q_{max}}$.

Adsorption kinetics model

The analysis of the adsorption kinetics model through testing using reaction equations of order 0, order 1, order 2, pseudo-order 1, and pseudo-order 2. The determination of which order equation is used is based on the R^2 value obtained from the linear regression equation. The Equation used is the one with the R^2 value closest to 1.

Equation of order 0

The reaction equation of order zero is presented in Equation 6.

$$C_t = C_0 - k_0 \cdot t \quad (6)$$

where: C_t is the concentration of the substance at time t (mg L^{-1}), C_0 is the concentration of the initial substance (mg L^{-1}), k_0 is the constant of the zero-order reaction rate (mg L^{-1} $minute^{-1}$), and t is the contact time of adsorption (minutes).

The zero-order reaction equation is obtained by plotting t on the x-axis and C_t on the y-axis, with slope = k_0 and intercept = C_0.

Equation of order 1

The reaction equation of order one is presented in Equation 7.

$$ln\ C_t = ln\ C_0 - k_1.t \quad (7)$$

where: C_t is the concentration of the substance at the time of t (mg L^{-1}), C_0 is the concentration of the initial substance (mg L^{-1}), k_1 is the constant of the reaction rate of order one ($minute^{-1}$), and *t* is the adsorption contact time (minutes).

The first-order reaction equation is obtained by plotting t as the x-axis and the value of $ln\ C_0/C_t$ as the y-axis, with slope = k_1.

Equation of order 2

The reaction equation of order two is presented in Equation 8.

$$\frac{1}{C_t} + \frac{1}{C_0} = k_2 \cdot t \quad (8)$$

where: C_t is the concentration of the substance at the time of *t* (mg L^{-1}), C_0 is the concentration of the initial substance (mg L^{-1}), k_2 is a second-order reaction rate constant (g mg^{-1} $minute^{-1}$), and *t* is the adsorption contact time (minutes).

A second-order reaction equation is obtained through the plot of t as the x-axis and the value $\frac{1}{C_t}$ as the y-axis, where slope = k_2 and Intercept = $\frac{1}{C_0}$.

Pseudo-order equation 1

The pseudo-order equation 1 is presented in Equation 9.

$$\log (q_e - q_t) = \log q_e - \frac{k_1}{2.303} \cdot t \quad (9)$$

where: q_e is the capacity for metal ion equilibrium, namely the weight of cadmium ions adsorbed per unit weight of ACCF (mg g^{-1}), q_t is the capacity for cadmium ion at time t, namely the weight of cadmium ions adsorbed per unit weight of ACCF (mg g^{-1}), is the pseudo first-order

adsorption rate constant (minute^{-1}), t is the adsorption contact time (minute).

The first-order pseudo reaction equation is obtained by plotting t as the x-axis and the log value ($q_{e\_}q_t$) as the y-axis, with slope = $\frac{k_1}{2.303}$ and intercept = log q_e.

Pseudo-order equation 2

The pseudo-order Equation 2 is presented in Equation 10.

$$\frac{t}{q_t} = \frac{1}{k_2 \cdot q_e^2} + \frac{1}{q_e} \cdot t \quad (10)$$

where: q_e is the capacity for metal ion equilibrium, namely the weight of cadmium ions adsorbed per unit weight of ACCF (mg g^{-1}), qt is the capacity for cadmium ion at time t, namely the weight of cadmium ions adsorbed per unit weight of ACCF (mg g^{-1}), is the second order pseudo adsorption rate constant (g mg^{-1} minute^{-1}), t is the adsorption contact time (minute).

The Equation of the pseudo-second reaction is obtained through a plot of t as the x-axis and $\frac{t}{q_t}$ as the y-axis, with slope = $\frac{1}{q_e}$ and intercept = $\frac{1}{k_2 \cdot q_e^2}$.

RESULTS

Results of the activated carbon characteristics test

Activated carbon that has been chemically activated and chemically-physical activation are both tested for moisture content, volatile matter, ash content, and iodine number, and the fixed carbon is calculated using Equation 1. The test results are presented in Table 2.

Table 2 shows that chemically activated carbon alone does not meet the SNI 06-3730-1995 standard for fixed carbon parameters, whereas chemically and physically activated carbon meet the SNI standards. Furthermore, the BET results showed that ACCF has a surface area of 394.7785 m^2 g^{-1} and an average pore diameter of 6.9084 nm. The surface area of ACCF activated with HCl was slightly lower than that of H_3PO_4 (Njoku et al., 2014). Meanwhile, the results of the FTIR test are presented in Figure 2.

The results of FTIR analysis on Activated Carbon from Coconut Fronds (ACCF) are shown in Figure 1a. The spectrum shows several major absorption peaks at 2362.716 cm^{-1}; 1123.525 cm^{-1}; 873.229 cm^{-1}; and 541.417–556.662 cm^{-1}. The peak at 2362.716 cm^{-1} is generally associated with the uptake of atmospheric CO_2 gas during sample preparation. A significant absorption band at 1123.525 cm^{-1} indicates the presence of a C–O strain of the alcohol, ether, or phenol functional group. This oxygen functional group plays a vital role as an active site for ion exchange and for the formation of surface complexes with Fe^{2+} and Mn^{2+} metal ions during adsorption. The peak at 873.229 cm^{-1} corresponds to the C–H bending vibration of the substituted aromatic ring, which indicates the formation of a stable aromatic structure after the carbonization process. Meanwhile, absorption bands in the range of 541–556 cm^{-1} indicate vibrational deformation of C–C and C–O–C in conjugated and graphinized carbon tissues.

The absence of a typical wide absorption band in the area of 3400–3600 cm^{-1} (strain O–H) and a sharp band at around 1700 cm^{-1} (strain C=O) suggests that the thermal activation process at 923 K after treatment with HCl has successfully degraded and aided most of the labile polar function activities through intensive dehydrogenation and deoxygenation reactions. This results in a more condensed carbon structure that is hydrophobic

Table 2. Parameters of activated carbon

No	Parameter	ACCF with chemical activation	ACCF with chemical and physical activation	Standard*
1	Water content (%)	11	5	Max 15
2	Volatile matter (%)	21	14	Max 25
3	Ash content (%)	9	5.1	Max 10
4	Fixed carbon (%)	59	71	Min 65
5	Iodine number (mg g^{-1})	830.6	1130.26	Min 750

Note: *SNI 06-3730-1995.

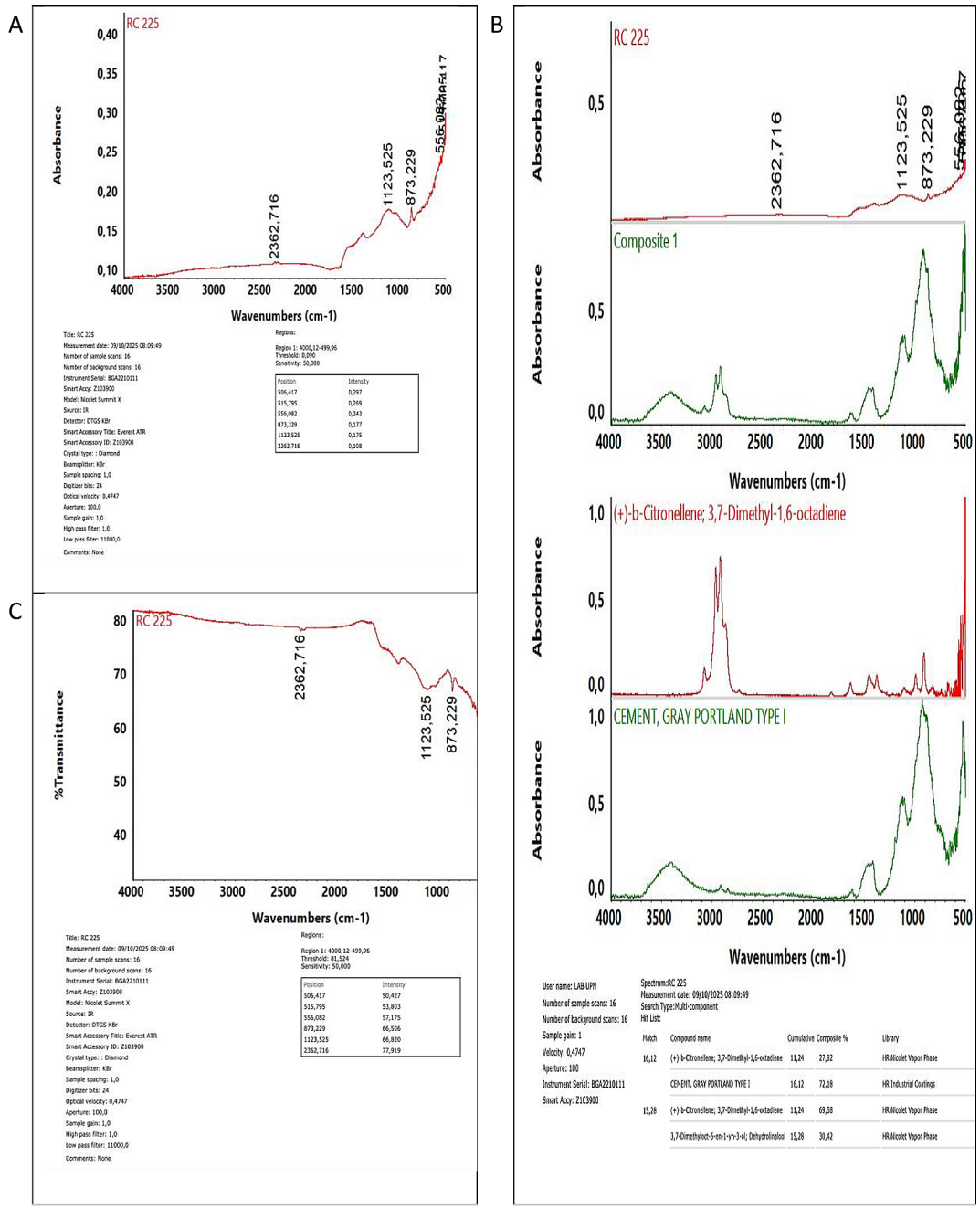

Figure 2. ACCF FTIR test results: (a) abs peak, (b) match, (c) trans peak

and highly carbonized. C-O groups are also found in activated carbon derived from coconut shells (Ojo et al., 2025). The effectiveness of chemical-physical activation with HCl and high temperatures in this study was shown to be superior at creating graphitic carbon structures and reducing labile polar groups, thereby increasing surface area and thermal stability.

The ACCF in this study indicates that the formation of carbonized structures is quite good. This condition is reflected in the dominance of the peak in the strong fingerprint area (< 1500 cm^{-1}), which is directly accumulated by the increase in the BET surface area value (394.78 $m^2\ g^{-1}$) and the iodine number (1130.26 mg g^{-1}). This second value is higher than the value reported by Chuein et al. using KOH activators. The combination of chemical activation (HCl) and thermal activation (923 K) for ACCF synthesis was shown to synergistically enhance micropore formation, strengthen the graphite structure, and maintain stable C–O groups as the main active sites (Chuein et al., 2021).

Overall, the FTIR profile of ACCF reveals an optimal composition of the surface functional group, which is dominated by the C–O (ether/alcohol), aromatic C–H, and C–O–C groups. These compositions support the chemical adsorption mechanism (chemisorption) by forming a coordinating bond between the metal ions Fe^{2+} and Mn^{2+} and the electron-donor oxygen atoms on the carbon surface. This stable function group configuration and high surface area collectively explain the high removal efficiencies for Fe (83.33%) and Mn (66.88%), while demonstrating improved ACCF performance compared to other biomass-based adsorbents reported.

In addition to the findings from the clusters contained in activated carbon, the study also reported findings from the activated carbon surface after chemical activation and chemical-physical activation, as presented in Figure 3.

Figure 3a shows that the activated carbon after chemical activation has a cleaner surface than the impurities. However, it is still relatively smooth, with small pores (micropores) beginning to appear; there are not many of them. The surface structure is not too open because there has been no physical activation process to expand the pores. Furthermore, Figure 3b) shows that the activated carbon surface appears hollow and coarse, with the pores wide open. Micropores and mesopores are formed evenly, and pore channels form, increasing the access of molecules to the inner surface.

In addition to the activated carbon surface, the EDS-SEM test also provides information on the surface morphology of activated carbon (Figure 4) and the content of activated carbon elements after chemical activation and physical-chemical activation (Figure 5).

Figure 4a shows the surface morphology of activated carbon after chemical activation, i.e., the surface of activated carbon is uneven in the presence of layered structures and porous areas. The surface of activated carbon is not homogeneous; it contains dark and light areas that indicate differences in topography or elemental composition. Meanwhile, Figure 3b shows that the surface morphology of activated carbon after chemical and physical activation is greater than that of chemically activated carbon alone (Figure 4a). On the surface of the chemically and physically activated carbon (Figure 4b), there are more and deeper pores than in Figure 4a, and the structure is irregularly shaped and rough, indicating effective activation. Some parts show rod-like structures or long slabs, which are lignocellulose residues (cellulose/lignin that are not fully carbonized). The presence of delicate and large pores (micro- and mesoporous) indicates that the chemical and physical activation process has opened the surface of the activated carbon, increasing its surface area. This rough, hollow surface is essential for improving the adsorption capacity of Fe and Mn ions. Figure 4b also shows agglomeration (clumping) in some areas that may be caused by mineral residues or the reaction of chemical activators, HCl.

A morphological comparison between the chemically activated carbon of Figure 4a and the combined chemical-physical activation of Figure 4b shows significant changes in its surface structure. Chemically activated ACCFs have a relatively smooth surface with small pores (micropores) beginning to form, but these pores are not evenly distributed. Some areas are still covered by residue or have not been fully carbonized. In contrast, chemically activated ACCFs

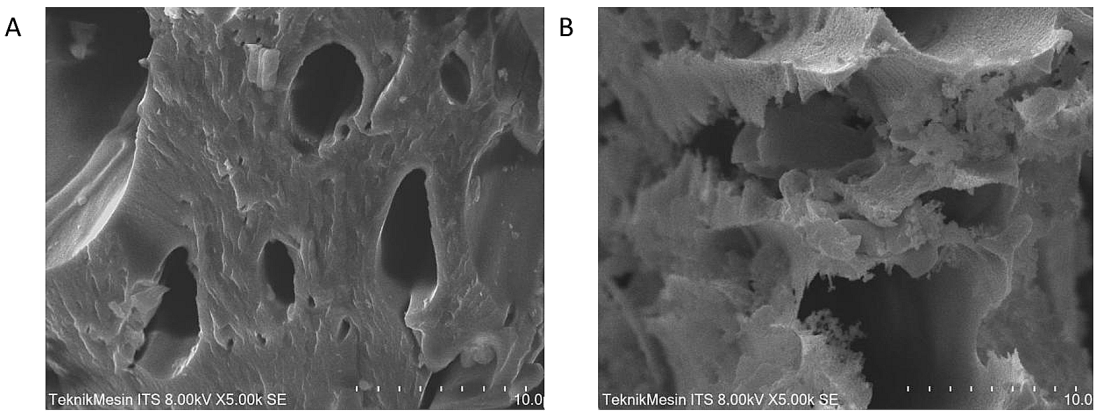

Figure 3. Surface activated carbon (5000x): (a) after chemical activation, (b) after chemical-physical activation

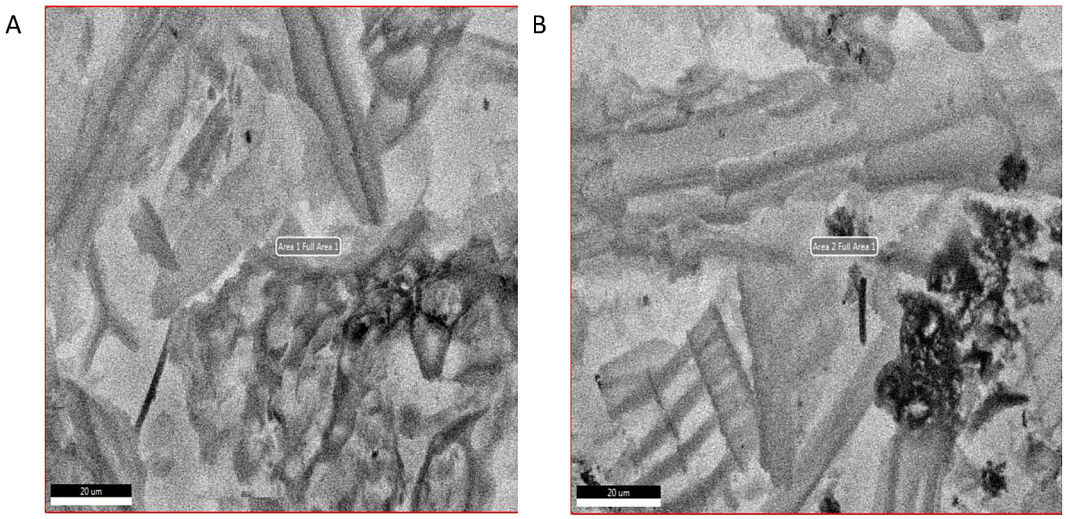

Figure 4. Surface morphology of activated carbon: (a) after chemical activation, (b) after chemical-physical activation

and surface-activated ACCFs appear rougher, layered, and hollow, with more micropores and mesopores, and are interconnected. Pore channels form due to gasification during heating at 923 K, increasing the effective surface area and the accessibility of metal ions during adsorption.

Elemental composition (EDX)

EDX analysis showed significant changes in the composition of the activated carbon element after the combined activation treatment, as presented in Figure 5 and Table 3.

Based on the SEM-EDX results in Figure 5 and Table 3, the increase in carbon (C) content from 70.45% to 74.75% after combined activation confirms that the thermal process is effective in removing volatile compounds and increasing carbonization. This happens because heating at high temperatures (923 K) decomposes non-carbon components such as hemicellulose, cellulose, and some lignins, resulting in a more polymerized aromatic structure. The decrease in oxygen (O) content from 26.68% to 15.34% indicates an intensive deoxygenation reaction, evidenced by the release of –OH, C=O, and C–O groups, which is common in the thermal activation process of lignocellulose-based carbon. This reaction results in a more hydrophobic, lower-energy surface, which enhances specific interaction with metal ions via the coordinating mechanism of the remaining aromatic oxygen.

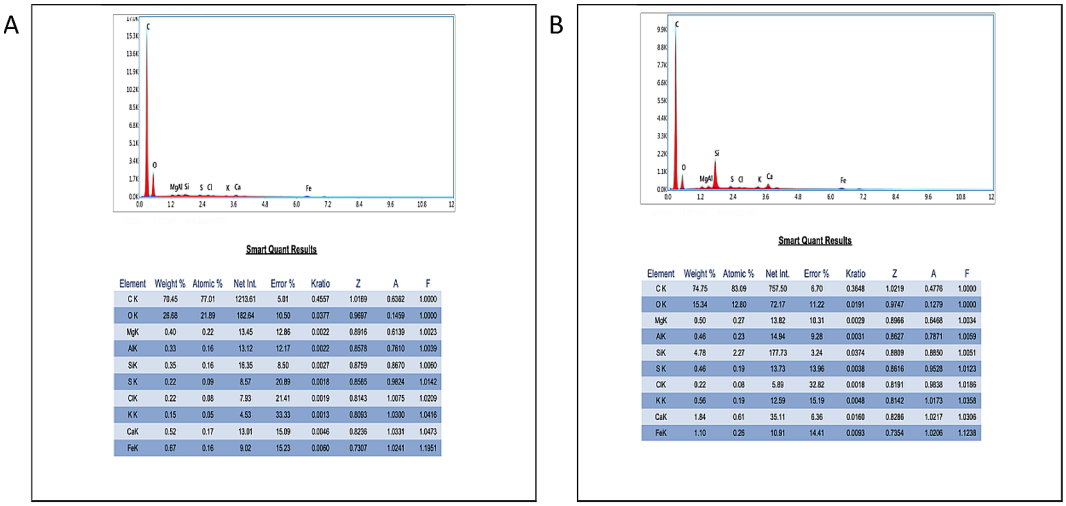

Figure 5. Elemental content of activated carbon: (A) after chemical activation, (B) after chemical-physical activation

Table 3. Comparison of the composition of ACCF with chemical activation and chemical and physical activation (%wt)

Element	Composition of ACCF with chemical activation (%wt)	Composition of ACCF with chemical and physical activation (%wt)	Percent change
C	70.45	74.75	5.8
O	26.68	15.34	-73.9
Si	0.35	4.78	92.7
Ca	0.52	1.84	71.7
Fe	0.67	1.1	39.1
others (Mg, Al, K, S, Cl)	<1	<1	-

The increased Si and Ca content indicates that the natural mineral residues in the coconut fronds (mainly silica and calcium oxide) do not fully decompose during activation. The presence of these two elements can strengthen the pore wall structure and slow the collapse of the carbon structure during heating, ultimately supporting the formation of a stable micropore network. Small amounts of Fe, K, and Mg can act as dopants, increasing surface acidity and strengthening electrostatic interactions with Fe^{2+} and Mn^{2+} ions in solution.

Thus, an increase in the C/O ACCF ratio after dual activation can be considered an indicator of successful carbonization and the formation of more regular micropore structures. Surfaces with a predominance of aromatic C–O–C and C–H groups provide an ideal balance between hydrophobicity and the presence of active sites, enabling chemical adsorption (chemosorption) via ion-exchange mechanisms or the formation of coordination bonds with Fe^{2+} and Mn^{2+}. Overall, these findings confirm that the combination of chemical-thermal activation is the most effective synergistic approach for improving the quality and adsorption capacity of activated carbon derived from coconut frond waste.

Correlation between surface morphology (SEM–EDX) and adsorption isothermal behavior

The SEM–EDX analysis showed that the combined activation process effectively increased the degree of carbonization of Activated Carbon from Coconut Fronds, as indicated by increases in carbon content from 70.45% to 74.75% and a simultaneous decrease in oxygen content from 26.68% to 15.34%. This transformation implies the removal of oxygenated functional groups, such as hydroxyl (–OH), carbonyl (C=O), and ether (C–O–C), resulting in a more orderly surface structure and the formation of graphite. The reduction of polar oxygen functionality and the formation of aromatic carbon networks created an energetically uniform surface, consistent with the experimentally observed Langmuir adsorption model (R^2 = 0.986). This shows that Fe(II) ions are mainly adsorbed as a single layer at a homogeneously distributed active site (Jasri et al., 2023). Further, the removal of volatile oxygen compounds during thermal activation not only improves carbon purity but also creates micropores and mesopores, thereby increasing surface area and pore connectivity. This structural modification facilitates the diffusion and accessibility of Fe(II) ions into the pore canal, thereby increasing the adsorption capacity (q_max = 432.6 mg g^{-1}). The presence of residual oxygen sites—although reduced—still contributes to specific coordination or ion exchange with Fe(II) ions, as supported by the moderate Langmuir constant (K_L = 0.0255 L mg^{-1}). This dual character of ACCF – combining high carbon purity with selective oxygenation sites – explains its strong adsorption performance and its compatibility with the Freundlich model (R^2 = 0.937), which accounts for surface heterogeneity. The surface composition detected by EDX confirms the presence of Si and Ca, which can cause local charge imbalances and strengthen the electrostatic interactions of Fe(II) ions. These findings are in line with previous research showing that mineral-doped carbon exhibits increased adsorption due to synergistic electrostatic and van der Waals forces (Jabbar et al., 2022; Abdul Manaf et al., 2022; Hammad et al., 2025).

Model adsorpsi isoterm

The results of the ACCF adsorption power test against Fe and Mn in modified acid mine drainage are presented in Table 4.

Table 4. Percentage of ACCF removal of Fe and Mn

Initial of Fe and Mn concentration (mg L^{-1})	Final concentration of Fe (mg L^{-1})	Final concentration of Mn (mg L^{-1})	Fe removal (%)	Mn removal (%)
600	220.41	230.13	63.27	61.65
525	176.63	200.45	66.36	61.82
450	136.63	150.09	69.64	66.65
375	75.68	124.11	79.82	66.90
300	50.01	99.35	83.33	66.88

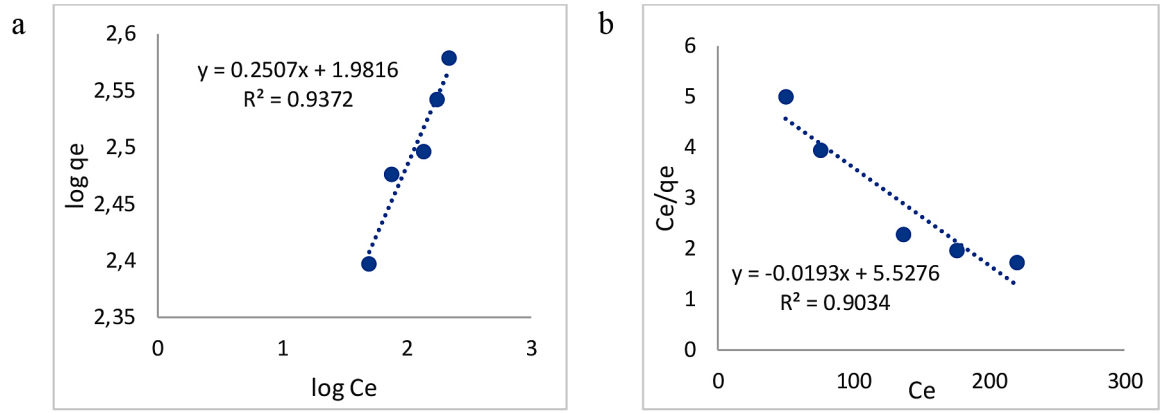

Figure 6. ACCF isothermal adsorption model against Fe: (a) Freundlich, (b) Langmuir

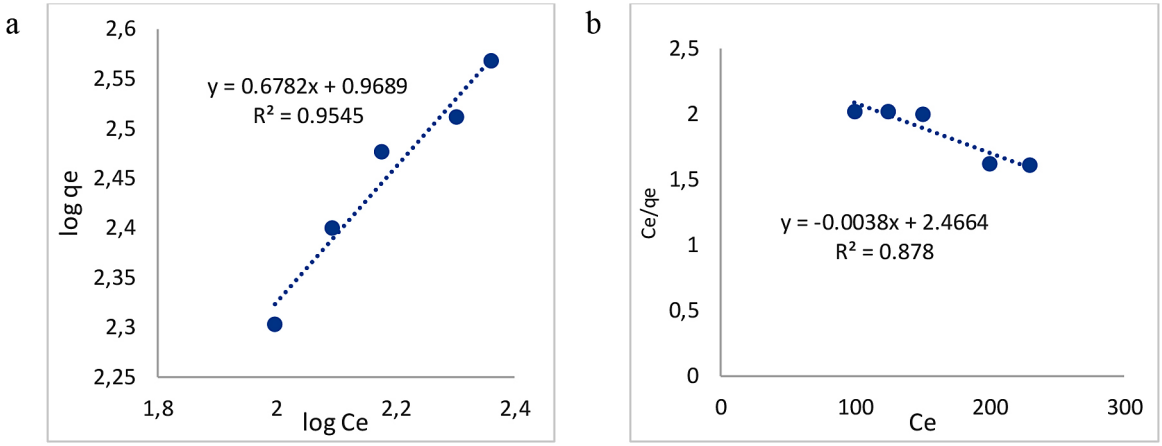

Figure 7. ACCF isothermal adsorption model against Mn: (a) Freundlich, (b) Langmuir

The isothermal adsorption model of ACCF against Fe and Mn was tested using the Freundlich and Langmuir equations. Based on Equation 3 and Table 4, a graph of the ACCF isothermal adsorption model was generated as a function of Fe (Figure 6). Meanwhile, from Equations 4 and Table 4, a graph of the ACCF isothermal adsorption model for Mn was obtained (Figure 7).

From Figures 6 and 7, the Freundlich and Langmuir constants are obtained as presented in Table 5. Based on Figures 6 and 7, it can be concluded that the Freundlich equation is more suitable for the ACCF isothermal adsorption model against Fe and Mn. This condition is because the surface of activated carbon is not homogeneous. The pore structure of activated carbon is composed of micropores and mesopores with varying size and depth, so that their adsorption energy also varies (Figure 3b). The Freundlich isotherm assumes adsorption on a heterogeneous surface with a non-uniform distribution of adsorption energies, which is consistent with the adsorbents used in this study. The presence of C–O (ether/alcohol), aromatic C–H, and C–O–C functional groups (Figure 2), pore size distribution, and surface irregularities

Table 5. Isotherm adsorption equation constant

Adsorption type	Constant	Constant value	
		Fe	Mn
Freundlich isothermal	R^2	0.9372	0.9545
	n	3.9888	1.4745
	k_f ((mg g^{-1})(L mg^{-1})^(n^{-1}))	95.8520	9.3089
Langmuir isotherm	R^2	0.9034	0.8780
	b (L mg^{-1})	-0.00349	-0.00154
	q_m (mg g^{-1})	-51.8135	-263.1579

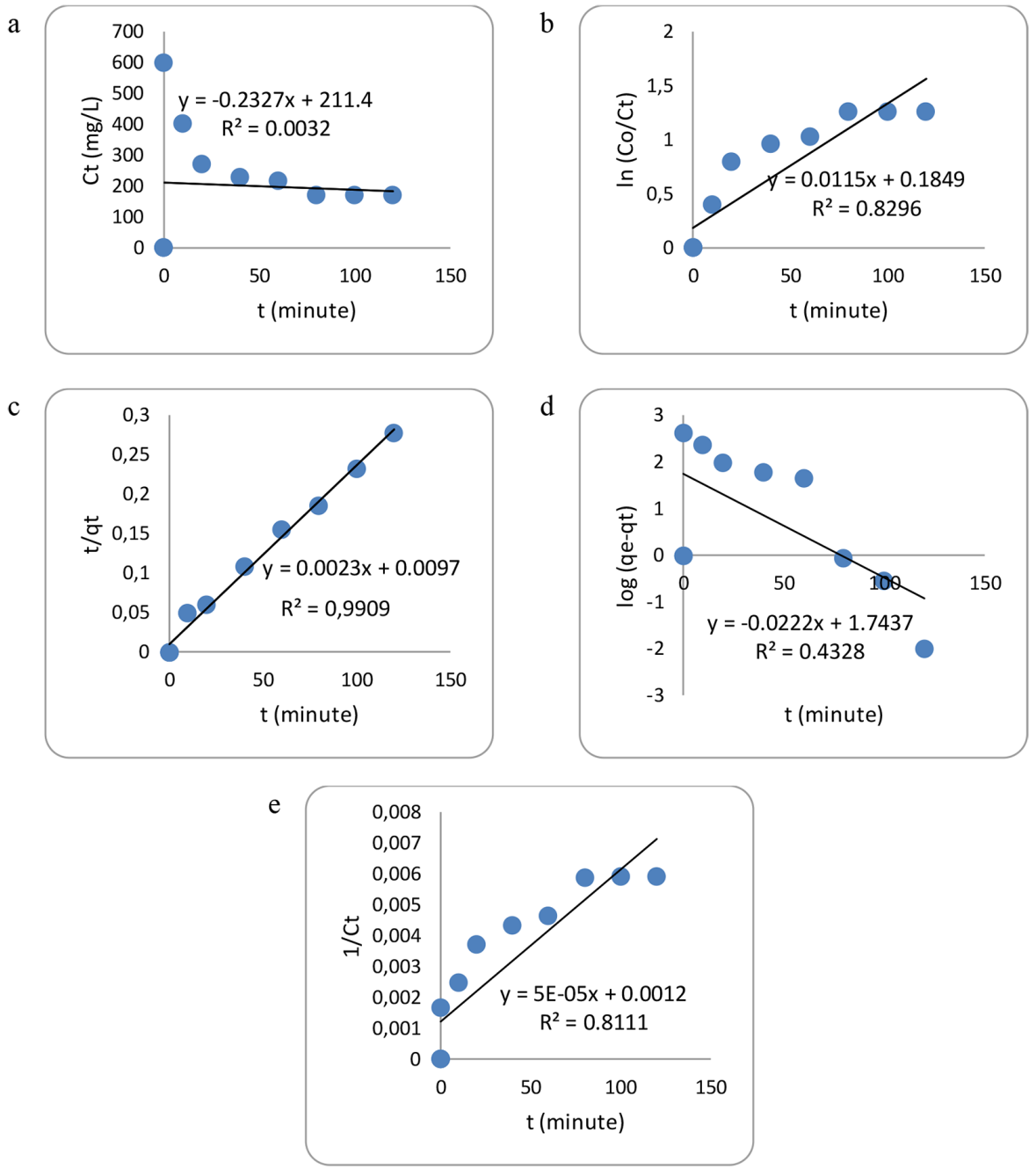

Figure 8. ACCF adsorption kinetics model of Mn: (a) order 0, (b) order 1, (c) order 2, (d) pseudo order 1, (e) pseudo order 2

Table 6. The constant of the kinetic Equation of adsorption

Adsorption kinetics	Constant	Constant value
Order 0	k_o (mg L^{-1} $minute^{-1}$)	0.2327
	R^2	0.0032
Order 1	k_1 ($minute^{-1}$)	0.0115
	R^2	0.8296
Order 2	k_2 (g mg^{-1} min^{-1})	0.00005
	R^2	0.8111
Pseudo order 1	pseudo k_1 ($minute^{-1}$)	0.0511
	R^2	0.4328
Pseudo order 2	pseudo k_2 (g mg^{-1} $minute^{-1}$)	0.0005
	R^2	0.9909

(Figure 3) contribute to multilayer adsorption and variations in adsorption site affinity.

In contrast, the Langmuir model assumes a homogeneous surface, identical adsorption sites, and monolayer adsorption without interactions between adsorbed molecules. The lower correlation coefficient obtained from the Langmuir model indicates that this assumption underrepresents the actual adsorption mechanism in this system. The deviation from the Langmuir behavior indicates that adsorption does not occur uniformly on a single type of active site, but rather on a heterogeneous surface with different binding energies.

Furthermore, the higher R^2 value of the Freundlich model compared to the Langmuir model confirms that surface heterogeneity plays a significant role in the adsorption process. This finding is consistent with previous studies reporting that adsorbents derived from natural or modified carbon-based materials tend to follow the Freundlich isotherm due to their complex surface structures. Therefore, based on the higher correlation coefficient and the underlying adsorption assumptions, the Freundlich model provides a more accurate representation of the adsorption behavior in this study (Kusdarini et al., 2025).

Adsorption kinetics model

The results of the test model of ACCF adsorption kinetics to Mn are presented in the Figure. 8. Tt can be concluded that the model of ACCF adsorption kinetics to Mn follows the pseudo-order equation 2. The equations of adsorption kinetics are presented in Table 6.

Table 6 shows that the value of the determination coefficient (R^2) of pseudo-order 2 is the highest compared to other orders, which is 0.9909 with a constant of 0.0005 g mg^{-1} $minute^{-1}$. That proved that ACCF has the same characteristics as active carbon from other biomass, as the kinetic model follows a pseudo-second-order reaction (Kusdarini et al., 2025; Ojo et al., 2025; Ni`mah et al., 2025). These findings show that Mn adsorption by ACCF is controlled by chemical adsorption, i.e., electron bonding or ion exchange between the active groups (C-O and C-O-C) on the surface of the activated carbon and Mn^{2+} ions in solution. Mn^{2+} ions have a high tendency to form coordination bonds with oxygen groups (C-O and C-O-C) on the surface of activated carbon.

CONCLUSIONS

Based on the objectives of this study, which aimed to synthesize and evaluate coconut frond–based activated carbon for Fe and Mn removal from acid mine drainage, the prepared adsorbent demonstrated strong potential for mine water remediation. The activated carbon produced through HCl chemical activation and thermal treatment at 923 K exhibited favorable physicochemical properties, including a high fixed carbon content (75.9%), a moderate specific surface area (394.78 m^2 g^{-1}), a mesoporous structure, and a high iodine number (1130.26 mg g^{-1}). These characteristics support its effective adsorption performance. The presence of C–O functional groups played a significant role in the adsorption mechanism, particularly through ion exchange interactions. Adsorption equilibrium data for Fe and Mn were best described by the Freundlich isotherm model, indicating multilayer adsorption on a heterogeneous surface. In contrast, the adsorption kinetics followed the pseudo-second-order model, suggesting that chemisorption

was the dominant rate-controlling mechanism. The maximum adsorption capacities reached 95.85 mg g^{-1} for Fe and 9.31 mg g^{-1} for Mn. Overall, the high removal efficiencies achieved (83.33% for Fe and 66.88% for Mn) confirm that coconut frond–based activated carbon effectively meets the research objectives and represents a low-cost, efficient, and sustainable alternative adsorbent for acid mine drainage remediation.

Acknownledgements

The authors thank the staff of the Chemical Engineering Process Laboratory, Institut Teknologi Adhi Tama Surabaya, Indonesia, for their support in developing this research.

REFERENCES

1. Abdul Manaf, S. F., Indera Luthfi, A. A., Md Jahim, J., Harun, S., Tan, J. P., Mohd Shah, S. S. (2022). Sequential detoxification of oil palm. *Cleaner and Circular Bioeconomy, 6.*
2. Fronds hydrolysate with coconut shell activated charcoal and pH controlled in a bioreactor for xylitol production. *Chemical Engineering Research and Design*, *179*, 90–106. https://doi.org/10.1016/j.cherd.2022.01.008
3. Atilano-Camino, M. M., López, L. R., Lozano, N. G., Hernández-Eligio, A., Vega-Alvarado, L., Juárez, K., Molina Freaner, F. E., Pat-Espadas, A. M. (2026). Enhanced metal removal from acid mine drainage using manganese- and quinizarin-modified Biochar in constructed wetlands. *Journal of Water Process Engineering*, *81*, 109209. https://doi.org/10.1016/j.jwpe.2025.109209
4. Bafounga, Y., Bourdelle, F., Claisse, P., Ventalon, S., Hofmann, A., Lloret, E. (2025). Mineralogical evidence of acid mine drainage on spoil tips of the Nord Pas-de-Calais coal mining basin (Northern France): A high-resolution characterization of the black shale weathering. *Chemical Geology*, *698*, 123132. https://doi.org/10.1016/j.chemgeo.2025.123132
5. Budianto, A., Kusdarini, E., Amrullah, N. H., Ningsih, E., Udyani, K., Aidawiyah. (2021). Physics and chemical activation to produce activated carbon from empty palm oil bunches waste Physics and chemical activation to produce activated carbon from empty palm oil bunches waste. *IOP Conference Series: Materials Science and Engineering*, *1010*. https://doi.org/10.1088/1757-899X/1010/1/012016
6. Budianto, A., Kusdarini, E., Mangkurat, W., Nurdiana, E., Asri, N. (2021). Activated carbon producing from young coconut coir and shells to meet activated carbon needs in the water purification process. *Journal of Physics: Conference Series*.
7. Budianto, A., Pratiwi, A. G., Ningsih, S. A., Kusdarini, E. (2023). Reduction of ammonia nitrogen and chemical oxygen demand of fertilizer industry liquid waste by coconut shell activated carbon in batch and continuous systems. *Journal of Ecological Engineering*, *24*(7), 156–164. https://doi.org/https://doi.org/10.12911/22998993/164759
8. Camargo, F. C. F., de Carvalho Filho, C. A., Passos, R. G., Cota, S. D. S., Minardi, P. S. P., Bomtempo, V. L., de Ávila Navarro, T. F. (2026). Application of sulphur isotopes to investigate the generation and migration of acid mine drainage in a uranium mine. *Groundwater for Sustainable Development*, *32*, 101563. https://doi.org/10.1016/j.gsd.2025.101563
9. Chen, G., Zhu, G., Guo, J., Zhao, R., Gao, S. (2026). Rapid and self-stabilization leaching of pyrite using trichloroisocyanuric acid. *Applied Surface Science*, *723*, 165649. https://doi.org/10.1016/j.apsusc.2025.165649
10. Chuein, A. L. H., Idris, N. N., Hamidon, T. S., Azani, N. F. S. M., Abdullah, N. S., Sharifuddin, S. S., Ying, A. S., Hussin, M. H. (2021). Kinetics and equilibrium studies of methylene blue dye adsorption on oil palm frond adsorbent. *Desalination and Water Treatment*, *216*, 358–371. https://doi.org/10.5004/dwt.2021.26795
11. Fanani, Y., Paripurno, E. T., Cahyadi, T. A., Mushoffa, A., Korompis, A. E., Asmara, M. R. R., Yudwiantoro, D. F. (2025). Instrumentation and data-processing workflow for AMD neutralization: Linking rock formation, water-quality measurements, and index computation. *Indonesian Journal of Applied Physics*, *15*(2), 434477. https://doi.org/10.13057/ijap.v15i2.108469
12. Hammad, W. A., Alqahtani, F. M., Darweesh, M. A., Amr, M. H. A., Eweida, B., Bakr, A. (2025). Innovative methods using palm frond-derived activated carbon for Cu (II) adsorption. *Materials Chemistry and Physics*, *339*, 130568. https://doi.org/10.1016/j.matchemphys.2025.130568
13. Han, C., Cheng, X., Han, Z., Dai, S., Chen, Q., Nie, W., Han, Y., Zhu, H., Gao, X., Zhao, Y., Liu, F., Tucker, M. E., Meng, R. (2026). Effective bioremoval of Cu (II) and Sulfate from acid mine drainage via biomineralization with an extreme acidophile bacterium *V. pantothenticus* WL. *Journal of Contaminant Hydrology*, *277*, 104822. https://doi.org/10.1016/j.jconhyd.2025.104822
14. Hao, X., Hao, H., Bu, C., Long, E., Wang, H., Wu, P., Li, X. (2026). Temporal and spatial distribution, sources, and health risk assessment of trace elements in a typical karst river basin in Southwest China: Influence of acid mine drainage from abandoned coal mines. *Ecotoxicology and Environmental*

Safety, *309*, 119524. https://doi.org/10.1016/j.ecoenv.2025.119524

15. Jabbar, N. M., Salman, S. D., Rashid, I. M., Mahdi, Y. S. (2022). Removal of an anionic Eosin dye from aqueous solution using modified activated carbon prepared from date palm fronds. *Chemical Data Collections*, *42*, 100965. https://doi.org/10.1016/j.cdc.2022.100965
16. Jasri, K., Abdulhameed, A. S., Jawad, A. H., ALOthman, Z. A., Yousef, T. A., Al Duaij, O. K. (2023). Mesoporous activated carbon produced from mixed wastes of oil palm frond and palm kernel shell using microwave radiation-assisted K_2CO_3 activation for methylene Optimization by response surface methodology. *Diamond and Related Materials*, *131*, 109581. https://doi.org/10.1016/j.diamond.2022.109581
17. Kaliannan, K., Kaliannan, S. (2025). Adsorption of methylene blue dye using biochar derived from finger millet waste biomass: Kinetics, isotherms, and thermodynamic studies. *Global Nest*, *27*(9), 1–13.
18. Khumalo, R. D. S., Brink, H. G., Chirwa, E. M. N. (2025). Hydrothermal synthesis of aragonite from acid mine drainage (AMD) of the Witwatersrand basin in Gauteng, South Africa. *Minerals Engineering*, *234*, 109745. https://doi.org/10.1016/j.mineng.2025.109745
19. Kusdarini, E., Budianto, A. (2022). Characteristics and adsorption test of activated carbon from indonesian bituminous coal. *Journal of Ecological Engineering*, *23*(10), 1–15. https://doi.org/https://doi.org/10.12911/22998993/152343
20. Kusdarini, E., Budianto, A., Kusuma, M. N., Atiyatussa'adah, E. (2025). Adsorption capacity of magnetic activated carbon derived from snake fruit (*Salacca zalacca*) seeds to Cd(II): Characteristics and isotherm model. *Reaktor*, *25*(1), 12–18. https://doi.org/https://doi.org/10.14710/reaktor
21. Kusdarini, E., Hakim, L., Yanuwiadi, B., Suyadi, S. (2021). Study in the development of fixed bed filter adoption of public health of lake water users. *Walailak Journal of Science and Technology*, *18*(8), 1–10. https://doi.org/https://doi.org/10.48048/wjst.2021.9131
22. Kusdarini, E., Kusuma, M. N., Budianto, A., Atiyatussa'adah, E., Garino, E. A. (2025). Modification of activated carbon from processed salak fruit waste with Fe_3O_4 composite for removal of Pb(II) in wastewater. *Ecological Engineering & Environmental Technology*, *26*(1), 305–315. https://doi.org/https://doi.org/10.12912/27197050/196040
23. Kusdarini, E., Purwaningsih, D. Y., Budianto, A. (2021). Removal Pb2+ of Well Water using Purolite C-100 Resin and Adsorption Kinetic. *Pollution Research*, *40*(2).
24. Kusdarini, E., Sania, P. R., Budianto, A. (2023). Adsorption of iron and manganese ions from mine acid water using manganese green sand in batch process. *Journal of Ecological Engineering*, *24*(12), 158–166.
25. Kusdarini, E., Sania, P. R., Budianto, A. (2024). Netralisasi Air Asam Tambang Menggunakan Pengolahan Aktif dan Pasif. *Jurnal Ilmu Lingkungan*, *22*(3), 808–815. https://doi.org/10.14710/jil.22.3.808-815
26. Kusdarini, E., Yanuwiadi, B., Hakim, L., Suyadi, S. (2020). Adoption model of water filter by the society of lake water users in dry land area, Gresik, East Java, Indonesia. *International Journal on Advanced Science Engineering Information Technology*, *10*(5), 2089–2096.
27. Lin, H., Li, X., Zhou, M., Dong, Y. (2025). In-situ suppression of acid mine drainage from non-ferrous metal mine waste rocks using microbially induced carbonate precipitation. *Journal of Environmental Sciences*. https://doi.org/10.1016/j.jes.2025.11.048
28. Mao, Q., Yan, B., Luo, L. (2026). A novel approach based on iron-manganese bio-oxidation process for acid mine drainage treatment: Performance and mechanism. *Process Safety and Environmental Protection*, *205*, 108195. https://doi.org/10.1016/j.psep.2025.108195
29. Meng, L., Yang, Y., Zhou, S., Wang, S., Wang, W., Tan, R., Wang, L., Wang, Q., Wu, X., Du, A., Liu, Q., Bate, B. (2025). Hydro-chemical performance of copper mine waste-based capillary barriers for acid mine drainage control in humid climates. *Journal of Rock Mechanics and Geotechnical Engineering*. https://doi.org/10.1016/j.jrmge.2025.10.011
30. Moyo, A., Parbhakar-Fox, A., Meffre, S., Cooke, D. R. (2025). Co-disposal of wood ashes and mine wastes to control acid and metalliferous drainage. *Environmental Research*, *286*, 122853. https://doi.org/10.1016/j.envres.2025.122853
31. Ni`mah, L., Juliastuti, S. R., Mahfud, M. (2025). Microwave-assisted synthesis, characterization, and performance assessment of lemongrass-derived activated carbon for removal of Fe and Mn from acid mine drainage. *Journal of Renewable Materials*, *13*(11), 2169–2190. https://doi.org/10.32604/jrm.2025.02025-0044
32. Njoku, V. O., Islam, M. A., Asif, M., Hameed, B. H. (2014). Preparation of mesoporous activated carbon from coconut frond for the adsorption of carbofuran insecticide. *Journal of Analytical and Applied Pyrolysis*, *110*, 172–180. https://doi.org/10.1016/j.jaap.2014.08.020
33. Ojo, D. T., Amuda, O. S., Salam, K. K., Oyediran, O. F., Yekini, B. B. (2025). Preparation and characterization of steam-activated and green alkali-activated carbon from coconut shells. *Next Nanotechnology*, *8*, 100198. https://doi.org/10.1016/j.nxnano.2025.100198
34. Ren, Z., Zhang, Y., Jiang, J., Wei, L., Song, H., Tan,

W., Li, Y., Shi, D., He, L., Qin, H. (2025). Research on the synergistic recovery of iron and electricity production performance in acid mine drainage using fuel cells. *Journal of Environmental Chemical Engineering*, *13*(6), 120154. https://doi.org/10.1016/j.jece.2025.120154

35. Romal, J. R. A., DeBraske, E. (2025). Recoverable critical minerals from an acid mine drainage in Southern Wisconsin: Insights on the rare earth elements recovery using PuroliteTM C160 resin. *Journal of Water Process Engineering*, *79*, 108906. https://doi.org/10.1016/j.jwpe.2025.108906
36. Sales, C. F., Moreira, D. P., de Souza, S. M., Rizzo, E., Melo, R. M. C. (2025). Mining waste induces oxidative stress, cell death, and irreversible histopathology in the liver of Psalidodon rivularis in a contaminated Neotropical stream. *Environmental Research*, *281*, 121974. https://doi.org/10.1016/j.envres.2025.121974
37. Singer, D. M., Izworski, R., Dudik, A., Tessin, A. C. (2026). Seasonal variability in the hydrogeochemical behavior and metal fluxes of acid mine drainage: Implications for long-term output and treatment. *Journal of Contaminant Hydrology*, *277*, 104818. https://doi.org/10.1016/j.jconhyd.2025.104818
38. Tao, H., Ma, L., Lin, L., Zhang, J., Liu, P., Zhou, J., Wang, X. (2026). Synergistic sulfidation, biomineralization, and neutralization enhancing efficient copper recovery and sustainable remediation of acid mine drainage. *Journal of Environmental Chemical Engineering*, *14*(1), 120569. https://doi.org/10.1016/j.jece.2025.120569
39. Vega Garzon, L. P., Moreno, P., Camargo Millán, G. L. (2025). Performance of *Chlorella vulgaris* in iron removal from mildly neutralized acid mine drainage. *Case Studies in Chemical and Environmental Engineering*, 101316. https://doi.org/10.1016/j.cscee.2025.101316
40. Wibowo, Y. G., Safitri, H., Cahyani, K., Rohman, A., Sudibyo, S., Yuliansyah, A. T., Petrus, H. T. B. M., Kurniawan, S. B., Ramadan, B. S., Maryani, A. T., Syarifuddin, H. (2024). Enhanced modified magnetite bentonite-CaO/$FeCl_3$ from solid waste for highly efficient Methylene blue removal. *Global Nest*, *26*(4), 1–14.
41. Younis Al-Ani, Y. M., Ridha, A. M., Abbas, T. K., Ahmadlouydarab, M., Kamar, F. H. (2026). Modeling and enhanced biodiesel production using a sustainable green catalyst based on palm frond-activated carbon supported with zirconium oxide. *Fuel*, *403*, 136118. https://doi.org/10.1016/j.fuel.2025.136118